

# RANS Computational Fluid Dynamics Predictions of Pitch and Heave Ship Motions in Head Seas

Gabriel David Weymouth, Robert Vance Wilson, and Frederick Stern

*Iowa Institute of Hydraulic Research, University of Iowa, Iowa City, Iowa, USA*

---

This work extends the previous effort in unsteady Reynolds averaged Navier-Stokes (RANS) simulations developed by the ship hydrodynamics group of the University of Iowa Iowa Institute of Hydraulic Research to the capability to predict pitch and heave motions of ships with forward speed in regular head seas. The simulations are performed with CFDSHIP-IOWA, which is a general-purpose, multiblock, high-performance parallel computing RANS code. Numerical verification studies in space and time demonstrate convergence for nearly all variables. The modified Wigley hull form experimental data presented in Journee (1992) are compared with simulation results over a range of Froude numbers, wavelengths, and wave amplitudes and found to give accurate results, with uncertainties less than 2%. Viscous ship motions characteristics are investigated by decomposing the full nonlinear problem into the forward speed diffraction and pitch and heave radiation problems, in the manner of strip theory. Comparisons between the current viscous RANS solutions and those from experiments, strip theory, and nonlinear potential flow simulations show the RANS method to predict damping and added mass coefficients with a high degree of accuracy.

---

## Introduction

A SHIP IN SEAWAYS is a dynamic physical system. However, accounting for dynamic effects has generally been far removed from the actual design process due to the complexity of simulating unsteady flows. This difficulty has historically resulted in a separation of the fundamental aspects of ship analysis: resistance and propulsion, seakeeping, and maneuvering. Advanced predictive capabilities in each area, along with computational methods for optimization (Tahara et al 2000) will lead toward the realization of simulation-based design. This method will allow designers to efficiently meet the overall requirements of the ship hydrodynamics problem, likely revolutionizing the design process.

The majority of research has been devoted to the problem of steady resistance prediction due to its relative simplicity, but an accurate assessment of a ship's seakeeping characteristics is vital to its proper design. Among the first methods that provided accurate enough seakeeping results to be useful in the design process

was strip theory, first completely presented in Salvesen et al (1970). In strip theory, potential flow assumptions are coupled with small disturbance and response assumptions to simplify the fully nonlinear governing equations to two uncoupled sets of linear ordinary differential equations, one for vertical and one for horizontal plane motions. Generally, the results for vertical plane predictions have been much better than those for horizontal plane, but even pitch and heave predictions break down when the system violates the linear assumptions, such as for steep waves or irregular hull geometries. Inviscid panel models, such as WAMIT (Newman 1988), were later developed in an attempt to alleviate some of the limitations of strip theory with marginal improvements. An inviscid desingularized time domain method, in which the singularity distribution is outside the computational domain, was developed at the University of Michigan to attempt to further deal with nonlinear problems (Beck et al 1994).

More recent research has been devoted toward predictions that are based on the solution of the viscous flow field. The great majority of this research has been devoted to analysis of roll motions due to the obviously viscous nature and poor strip theory predictions of this flow. Examples of three-dimensional roll simu-

---

Manuscript received at SNAME headquarters June 19, 2003; revised manuscript received April 2, 2004.

lation are given in Chen et al (2001) for a rolling ship, and Miller et al (2002) for a three-dimensional cylinder with bilge keels.

However, the goal of total six degree of freedom predicted motions should be kept in mind. A detailed investigation of the vertical plane modeling of viscous ship motions is the first step in establishing confidence in unsteady Reynolds averaged Navier-Stokes (RANS) simulations. In addition, such a simulation will provide details of the effects of the linear and inviscid flow assumptions made in the most widely used computational models. Previous work on three-dimensional simulations of vertical plane motions includes Sato et al (1999), who presented results for the Wigley hull and Series 60 hull, and Cura Hochbaum et al (2002), who gave results for the Series 60 hull and a practical container-ship geometry in head seas. However, neither work presented a completely thorough analysis, lacking verification and detailed physical parameter study. The present work builds on and extends the unsteady RANS code CFDSHIP-IOWA (Paterson et al 2003), which has been developed following a step-by-step approach, continually adapted and enhanced to meet the requirements of new and more complicated simulations. Wilson et al (2000) and Wilson and Stern (2002a) presented steady-state simulations of a surface combatant. Rhee and Stern (2001) and Wilson and Stern (1998) presented unsteady simulations of the forward speed diffraction problem. Wilson and Stern (2002b) presented simulations of prescribed and predicted roll motion for a surface combatant. In each case detailed, verification and validation (if data were available) of the simulation results were presented.

The objective of the present work is to extend this previous effort in unsteady RANS simulations to the capability to accurately predict vertical plane ship motions and to apply this ability to predict pitch and heave response for the modified Wigley hull form in regular head seas. This classical problem has a wealth of solutions, both experimental and from inviscid flow calculations, with which to compare over a range of physical parameters. A rigorous numerical verification and experimental validation of the extended ability will be performed.

The next objective is to carry out a detailed analysis to demonstrate not only well-known behavior of vertical plane ship motions, but also characteristics of unsteady viscous flows, which could not be present in any linearized or inviscid model. A comparison with strip theory methodology will be undertaken by decomposing the fully nonlinear ship motion problem into its forward speed diffraction and radiation components. Analysis of this information will help to evaluate the importance of nonlinear and viscous effects in the predicted motions results.

## Computational method

There are four distinct physical problems that are modeled in the current work: simple steady-state motion, forward speed diffraction, forward speed radiation, and predicted motion response to incident waves. In the forward speed diffraction case, the model moves with constant forward speed fixed in the design condition. However, a regular traveling wave is introduced into the fluid domain, resulting in an unsteady flow field around the hull. In the radiation problem there is no incident wave and the hull is forced to oscillate with prescribed harmonic motion in addition to the steady forward motion. In the predicted motions problem, the incident wave is introduced into the fluid domain, and the hull, moving forward with constant speed, is allowed to respond to the

resultant forces and moments with coupled pitch and heave motions. These motions are depicted in Fig. 1.

## Fluid dynamics

CFDSHIP-IOWA solves the RANS equations to model the fluid flow around the ship body. In Cartesian coordinates for an inertial system, the continuity and momentum equations in non-dimensional tensor form are

$$\frac{\partial U_i}{\partial x_i} = 0 \quad (1)$$

$$\frac{\partial U_i}{\partial t} + U_j \frac{\partial U_i}{\partial x_j} = -\frac{\partial \hat{p}}{\partial x_i} + \frac{1}{\text{Re}} \frac{\partial^2 U_i}{\partial x_j \partial x_j} - \frac{\partial}{\partial x_j} \overline{u_i u_j} \quad (2)$$

where  $U_i = (U, V, W)$  are the Reynolds-averaged velocity components,  $x_i = (x, y, z)$  are the independent coordinate directions,  $\hat{p} = [(p - p_\infty)/\rho U_0^2 + z/\text{Fr}^2]$  is the piezometric pressure coefficient,  $\overline{u_i u_j}$  are the Reynolds stresses that are a two-point correlation of the turbulent fluctuations  $u_i$ ,  $\text{Fr} = U_0/\sqrt{gL}$  is the Froude number, and  $\text{Re} = U_0 L/\nu$  is the Reynolds number. All equations are non-dimensionalized by reference velocity  $U_0$ , length  $L$ , fluid viscosity  $\nu$ , and density  $\rho$ .

## Computational implementation

For utilization in CFDSHIP-IOWA, the equations are transformed from the Cartesian coordinate  $(x, y, z, t)$  to a nonorthogonal curvilinear coordinate system  $(\xi, \eta, \zeta, \tau)$  by a partial transformation, leaving the velocity vectors in Cartesian form. The grid-velocity terms that result from this transformation in unsteady flows are calculated directly using finite difference expressions. Temporal discretization of the transformed governing equations uses second-order formulations for time accurate calculations, and first-order for steady-state calculations. The approach uses structured higher-order upwind finite-difference spatial discretization, pressure-implicit split-operator for velocity-pressure coupling, and two-equation  $k-\omega$  turbulence modeling with no wall functions.

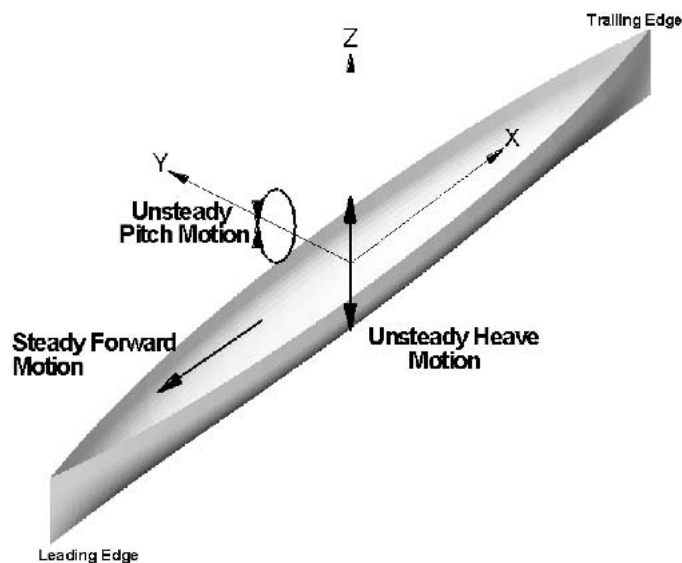


Fig. 1 Depiction of modeled motions

The ship motions problem represents a highly nonlinear initial boundary value problem (IBVP), with the steady-state solution used as the initial condition. Detailed descriptions of all the boundary conditions can be found in Paterson et al (2003). However, the unsteady free surface treatment will be discussed briefly.

### Free surface treatment, boundary, and initial conditions

CFDSHIP-IOWA makes use of a surface tracking method to model the fluid–air interface, where an exact two-dimensional kinematic free-surface boundary condition (KFSBC) is solved at each time step to predict the evolution of the free surface. The computational grid is then conformed to the free surface, and the RANS equations are solved in this fluid domain. The free surface location is then corrected based on the new velocity field, and the process repeats. This conforming process is illustrated in Fig. 2 at the midship section ( $x/L = 0.5$ ) of the modified Wigley hull. The grid on the left is unconformed, and the grid on the right has been conformed to the free surface elevation.

Twenty-six different boundary condition types are available in CFDSHIP-IOWA and are described in detail in Paterson et al (2003). Boundary conditions for the current unsteady simulations consist of inlet, exit, no-slip, symmetry, and far-field boundaries. For the forward speed diffraction and predicted motions problems, the incident wave elevation and velocity field are imposed onto the inlet boundary as boundary conditions for the two-dimensional KFSBC and RANS equations, from the linear potential flow solution for a free-surface traveling wave (Newman 1988). Conditions for wave elevation, velocity, and pressure are given by

$$\begin{aligned}\zeta(x,t) &= \zeta_a \cos(kx - \omega_e t) \\ U(x,z,t) &= \omega \zeta_a e^{kz} \cos(kx - \omega_e t) \\ W(x,z,t) &= \omega \zeta_a e^{kz} \sin(kx - \omega_e t) \\ p(x,z,t) &= \frac{\omega^2 \zeta_a}{k} e^{kz} \cos(kx - \omega_e t) - \frac{\omega^2 \zeta_a^2}{2} e^{2kz}\end{aligned}\quad (3)$$

where  $\zeta(x,y)$  is the unsteady free surface elevation,  $\zeta_a$  is the wave amplitude,  $U(x,z,t)$  is the axial velocity,  $W(x,z,t)$  is the vertical velocity, and  $p(x,z,t)$  is the pressure. The pressure gradient computed from the potential flow solution in equation (3) is used to set the pressure gradient at the inlet, which is required for solution of the pressure Poisson equation (i.e., a nonhomogenous Neumann condition for pressure). At the outflow, a convective boundary condition is used in the solution of two-dimensional KFSBC,

while the second derivative of the velocity field in equation (3) is used in the solution of the RANS equations at the exit. The non-dimensional wave number is defined as  $k = 2\pi/\lambda^*$ , where  $\lambda^* = \lambda/L$  is the non-dimensional wavelength. The non-dimensional wave encounter frequency is defined as  $\omega_e = \omega + k$ , where  $\omega$  is the wave frequency, which, for deep ocean waves, is  $\omega = (1/\text{Fr})\sqrt{2\pi}/\lambda^*$ . The non-dimensional linear encounter frequency  $f_e = \omega_e/2\pi$  can be written as a function of  $\text{Fr}$  and  $\lambda$ .

$$f_e = \frac{1}{\text{Fr}} \sqrt{\frac{1}{2\pi\lambda^*}} + \frac{1}{\lambda^*} \quad (4)$$

where  $f_e$  has been non-dimensionalized by  $U_0/L$ . The unsteady components for wave elevation, velocity, and pressure given in equation (3) are added to a steady-state solution (i.e., without motions and incident waves) to define initial conditions at  $t = 0$  for the unsteady simulations.

### Body coordinate system

Although the most basic reference system when dealing with Newtonian mechanics is a set of completely stationary coordinate axes known as the primary inertial system, it is often convenient to reference motion to a secondary nonstationary system. The first obvious choice for this secondary reference would be an accelerating body-fixed coordinate system, anchored at the center of gravity with axis embedded in the ship, as shown in Fig. 3a. When considering completely general motion, the body-fixed frame is regularly preferred over any other noninertial system as it eliminates possible dynamic cross-coupling effects due to internal moments.

However, in the case of the seakeeping problem, a secondary system can be chosen such that it moves with the ship at the constant velocity  $U_0$  but has no acceleration or rotation. Such a system is also inertial in nature and is shown in Fig. 3b. In the figure, the secondary system is anchored by reference point  $O$ ,  $\bar{x}_b$  is the vector from point  $O$  to the center of gravity of the model (CG), and  $\bar{\theta}_b$  is the rotation vector of the body relative to the inertial systems. The advantage of the nonaccelerating system is that the governing equations of motion are unchanged, whereas the accelerations of the body-fixed frame result in kinematic coupling of the degrees of freedom. In addition, because the constraints are inertial in nature for the seakeeping problem, additional restraint equations would need to be solved. For these simplifying reasons, a constant velocity inertial frame anchored at

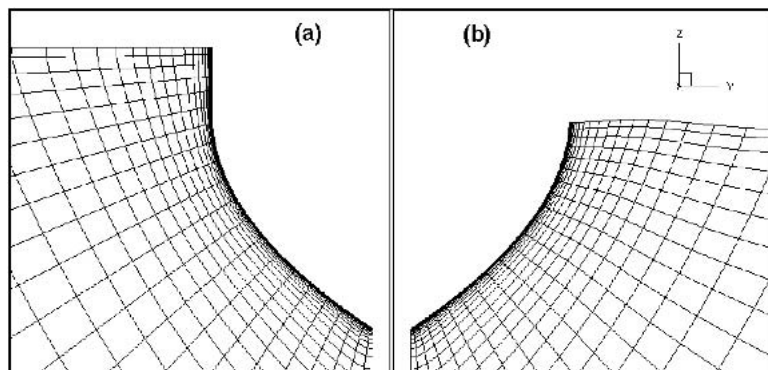


Fig. 2 Dynamic nonlinear surface tracking: (a) original grid, (b) conformed grid

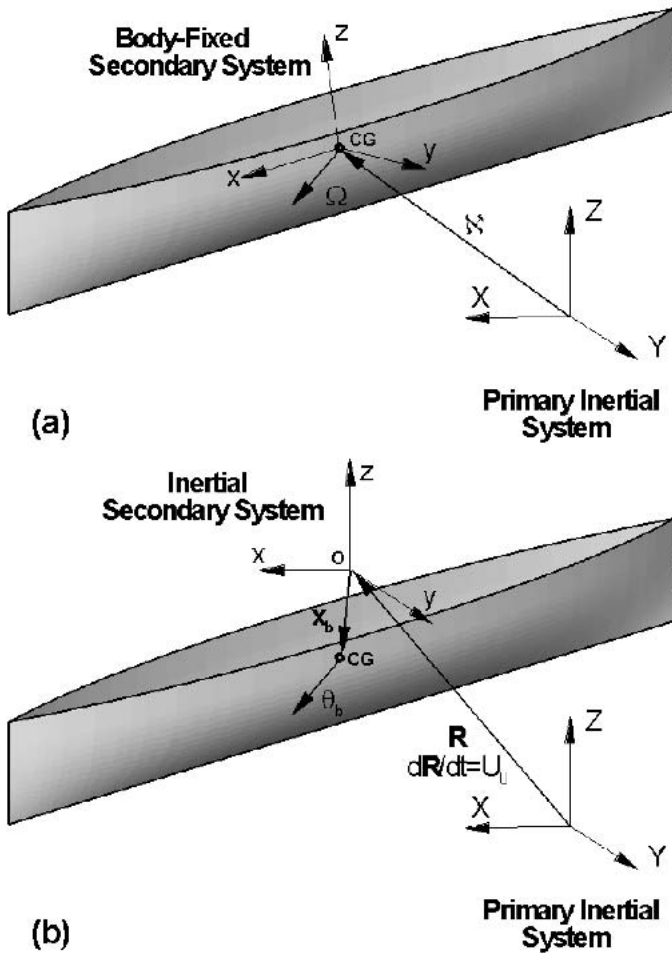


Fig. 3 Coordinate systems: (a) body fixed, (b) inertial

$\bar{x}/L = (0.5, 0, 0)$  was used in the current work. In addition, an inertial system was found to provide a more convenient reference for the majority of the fluid domain.

### Governing equations

The motion of a rigid constant-mass body relative to the inertial frame is governed by the conservation of linear and angular momentum, given in nondimensional tensor form simply by

$$\begin{aligned} \sum F_{bi} &= m \frac{d^2 x_{bi}}{dt^2} \\ \sum M_{bi} &= \frac{d}{dt} \left( I_{ij} \frac{d\theta_{bj}}{dt} \right) \end{aligned} \quad (5)$$

where  $m$  and  $I$  are the mass and moment of inertia tensor of the body,  $x_b$  and  $\theta_b$  are the translation and rotation of the body as shown in Fig. 3b, and  $\sum F_b$  and  $\sum M_b$  are the sum of the forces and moments acting on the body. The moment of inertia tensor  $I_{ij}$  is defined as

$$I_{xx} = \int_{V_b} \rho_b (y^2 + z^2) dV_b$$

$$I_{xy} = I_{yx} = - \int_{V_b} \rho_b (xy) dV_b \quad (6)$$

where  $\rho_b$  is the solid body density and  $V_b$  is the solid body volume, with exactly similar relations for the other terms in the tensor. Clearly, for a constant mass, nondeformable body such as our ship hull, the moment of inertia tensor is a function only of the coordinates system used in its calculation. Therefore, in a body-fixed system the tensor is constant. The program requires this tensor as an input. The transformation from this body-fixed-frame tensor to the inertial-frame tensor is given by

$$I_N = R_B^N I_B R_N^B + m X_B \quad (7)$$

where  $N$  and  $B$  refer to the inertial and body-fixed frame, respectively.  $X_B$  is the body translation matrix defined as

$$\begin{aligned} X_{b11} &= x_{b2}^2 + x_{b3}^2 \\ X_{b12} &= X_{b21} = -x_{b1} x_{b2} \end{aligned} \quad (8)$$

with similar relations for the other terms in the matrix.  $R$  is the cosine rotation matrix, the  $i, j$  component of which is defined as

$$R_{Bij}^N = \cos(i_B j_N) \quad (9)$$

where  $\cos(i_B j_N)$  is the cosine of the angle between the  $i$ -axis of the body-fixed frame and the  $j$ -axis of the inertial frame.

Accurate integration of the equations of motion in time was found to be of key importance to the correct prediction of motions. A third-order implicit integration scheme replaced the simple explicit first-order scheme that was initially implemented. For the small amplitude, two degree of freedom motions that are the focus of the current work, the time derivative of the moment of inertia tensor was always less than three orders of magnitude smaller than the steady term, and neglected.

### Forces and moments

The sum of the forces and moments acting on the ship are defined as

$$\begin{aligned} \sum F_b &= F_f + F_{pp} + F_{hp} + F_{mg} \\ \sum M_b &= M_f + M_{pp} + M_{hp} + M_{mg} \end{aligned} \quad (10)$$

where  $f$  refers to the skin friction,  $pp$  refers to the piezometric pressure,  $hp$  refers to the hydrostatic pressure, and  $mg$  refers to the weight. All of the moments must be taken relative to the inertial frame reference point  $O$  depicted in Fig. 3b. In equations (10), the effect of gravitational acceleration is the only body force considered, with magnetic and other possibly nonconservative body forces neglected.

The forces are integrated with a summation of the area elements based on the Jacobian of the coordinate transformation. This integration scheme was found to be second-order accurate, which is sufficient considering the accuracy of the main flow solver. The integration of the moments was also taken as a summation, with the center of force assumed to be the centroid of each elemental area.

## Overall solution procedure

The overall procedure for 6DOF simulations is outlined in Fig. 4. Steps 1 through 6 represent the time loop of the solution process. Steps 2 to 5 represent the inner loop. Based on previous studies (Wilson & Stern 1998, Wilson & Stern 2002b) and preliminary tests, it was determined that four inner iterations were sufficient for convergence and to produce time-accurate simulations for unsteady flows.

## Data, conditions, and geometry

### Comparison data

The Delft University of Technology report by Journee (1992) is used as the primary source of comparison data for the current work. Experimental measurements taken during forward speed diffraction, pitch and heave radiation, and free pitch and heave response tests are presented. Journee also supplies theoretical results from two strip-theory-based methods and uses the results from his experimental results to compute the equivalent coefficients that would be used in strip theory. The “original” strip theory results presented in Journee are based on the method detailed in Salvesen (1970). The “three-dimensional hybrid” results were computed based on the zero forward speed code WAMIT and corrected for forward speed using Salvesen et al (1970).

Rhee and Stern (2001) provide comparison data in the form of previous RANS simulations for the Wigley hull steady-state and forward speed diffraction problems. Rhee and Stern (2001) also included a comparison of his results for the unsteady forces acting on the hull with those of the inviscid program SWAN. To include comparisons with more advanced inviscid flow methods, the non-linear time-domain prescribed pitch and heave results presented in Beck et al (1994) are also considered. In that paper, Beck et al (1994) makes an analysis similar to the one presented in Journee, using radiation tests to back out the equivalent hydrodynamics coefficients for use in strip theory.

### Test conditions

The free response test matrix is shown in Table 1 with the base case values given in the first subtable. The base case physical

**Table 1 Predicted motion model test matrix**

	Fr	$\lambda/L$	$\zeta_a/L^*$	Grid Points	Time Steps/Wave
Base case values	0.3	1.25	3.67	~290K	70
Parameter values					
L	0.2	0.75	3.67	~110K	70
M	0.3	1.25	—	~180K	100
H	0.4	2.0	6.67	~290K	140
Parameter Studies					
Study	Fr	$\lambda/L$	$\zeta_a/L$	Grid Points	Time Steps/Wave
Fr	L,M,H	M	L	H	L
$\lambda$	M	L,M,H	L	H	L
$\zeta_a$	M	L	L,H	H	L
Grid	M	M	L	L,M,H	M
$\Delta t$	M	M	L	H	L,M,H

\*Value  $\times 10^3$ .

parameters were chosen to match the conditions Journee reported to be resonant in order to show that the current model would be able to predict the peak responses. Systematically varying the parameters from the base conditions generated five parameter studies with three physical (Fr,  $\lambda$ ,  $\zeta_a$ ) and two numerical (grid and time step) studies. *L*, *M*, *H* refers to low, medium, and high parameter values, respectively. A total of 10 simulations were required to generate the five parameter studies: three for Fr; two extra for  $\lambda$ ; one extra for  $\zeta_a$ ; two extra for the grid study; and two extra for the time step study.

In addition to the predicted motion tests, forward speed diffraction (FSD), prescribed heave radiation (PHR), and prescribed pitch radiation (PPR) simulations were performed. In the pitch and heave radiation cases, the prescribed oscillations are defined by

$$\begin{aligned} x_{b3} &= f(t)z_a \cos(\omega_p t) \\ \theta_{b2} &= f(t)\theta_a \cos(\omega_p t) \end{aligned} \quad (11)$$

where  $z_a$  and  $\theta_a$  are the amplitudes of the heave and pitch motions and  $\omega_p$  is the prescribed frequency.  $f(t)$  is a ramping function to smooth the transition into motion from the steady-state initial conditions, minimizing the transient response. The base case Froude number, grid, and time step were used in all three tests, but as Journee did not use the same wave height and length for his FSD and predicted motions experiments, these parameters do not match the base case conditions. These parameters are shown in Table 2. In summary, 13 total simulations were performed.

### Test geometry

This work limited itself to the simulation of the model labeled Wigley III by Journee. The physical properties of that model were taken from his report and are reproduced in Table 3 and Fig. 5.

The 10-block coarse computational grid is shown in Fig. 6 with dark lines indicating the block boundaries and the lighter lines indicating the internal grid lines. Due to the symmetry of this problem, the computational domain covers only the starboard side

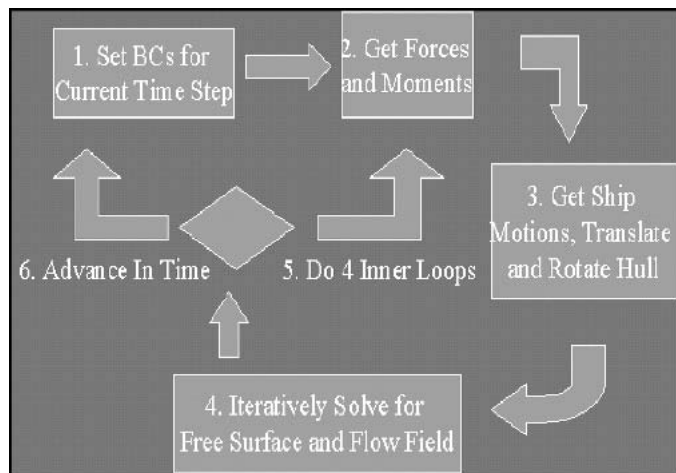


**Fig. 4** Overview of solution procedure. BCs = boundary conditions

**Table 2 Prescribed motion test matrix**

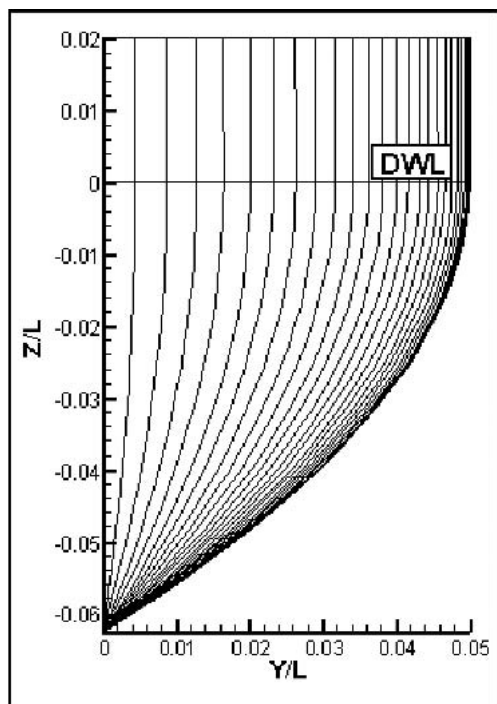
	$\zeta_d/L^*$	$\lambda/L$	$z_d/L^*$	$\theta_d$	$\frac{\omega_p}{\sqrt{g/L}}$
FSD	8.67	1.00	0	0	—
PHR	0	—	8.33	0	2.78
PPR	0	—	0	1.5 deg	2.76

\*Value  $\times 10^3$ .

FSD = forward speed diffraction; PHR = prescribed heave radiation; PPR = prescribed pitch radiation.

**Table 3 Wigley III model static properties**

Length (m)	3.000
Breadth (m)	0.300
Draft (m)	0.1875
Trim (m)	0.0
Volume of displacement, $\nabla$ (m <sup>3</sup> )	0.0780
Midship section coefficient, $C_m$	0.667
Wetted surface area, $S$ (m <sup>2</sup> )	1.350
Waterplane area, $A_w$ (m <sup>2</sup> )	0.624
Waterplane pitch moment of inertia, $I_{Ay}$ (m <sup>4</sup> )	0.2931
Center of rotation above baseline (m)	0.1875
$C_G$ above baseline (m)	0.170
Pitch radius of inertia, $k_{yy}$ (m)	0.750

**Fig. 5** Wigley III body plan

of the ship. This grid was required to meet a variety of constraints for accurate prediction of the boundary layer, free-surface, and motions. In order to resolve the turbulent boundary layer at the no-slip surface, a near-wall grid spacing of  $4.0 \times 10^{-6}$ ,  $3.3 \times 10^{-6}$ ,

and  $2.8 \times 10^{-6}$  is used on the coarse, medium, and fine grids, respectively. This results in a normalized near wall spacing of  $y^+ = 1, 0.84$ , and  $0.71$  on coarse, medium, and fine grids. The grid spacing at the inlet plane is smaller than that required for steady flow in calm seas due to the requirement of at least 25 points per wave needed to resolve the incident wave for even the shortest wavelength ( $\lambda/L = 0.75$ ). From the lower view in the figure it can be seen that the block separation lines fore and aft of the hull have been tilted downward. This allows the ship to trim without any block rising completely above the instantaneous free surface level. Were this to happen, grid conformation would be impossible, and in fact, this plane should be kept as far from the free surface as possible to minimize distortion of the grid due to conforming. The refinement ratio between grids was set as  $r_G = 2^{1/4}$  to help ensure the same level of physics was resolved on all grids.

## Uncertainty analysis

With the increased demands in the complication of simulated models and the accuracy of their results, sophisticated methods are needed to assess the quality of the computational fluid dynamics (CFD) simulations. Verification and validation processes used in this work follow the methodology and procedures presented in Stern et al (2001). Applications to a nonlinear flat plate analytical benchmark as well as detailed discussion of noninteger grid refinement ratios can be found in Weymouth (2002).

Briefly, the error in a simulation, that being the difference between the “true” answer and the simulation result, can be decomposed into its numerical and modeling components. Numerical errors, caused by finite values of discretization parameters, such as time step, are assessed by systematically refining the parameter while all others remain constant. Using generalized Richardson extrapolation, the order of accuracy  $r$ , the error in the solution  $d$ , and the uncertainty in the solution  $U$  can be estimated. For careful studies, the estimated error can be used to correct the solution and give corrected uncertainty  $U_c$ .

Modeling errors, caused by estimations made in developing and implementing the governing equations and boundary conditions of the physical system, are assessed by comparisons to experimental solutions. The difference between the simulation and the data is the comparison error  $E$ . This is compared to the validation uncertainty  $U_v$ , which is made up of the numerical uncertainty and the uncertainty in the data  $U_d$ . If the error is less than the uncertainty, the model is validated.

## Results

Discussion and analysis of the unsteady Wigley hull simulation results are presented in this section. First, the results of the verification and validation tests are presented, then the complete nonlinear predicted motions simulations results, and finally the forward speed diffraction and forward speed pitch and heave radiation results. Simulations were run for 10 to 12 encounter wave periods. Time histories of the forces, moments, and motions were recorded for the duration of the simulation, while the velocity and pressure fields over the full domain were recorded only for the final one to two encounter waves.

The force and moment coefficients are designated  $C_i$ , where  $i$  is the degree of freedom, with  $i = 1, 3$  for forces and  $i = 4, 6$  for

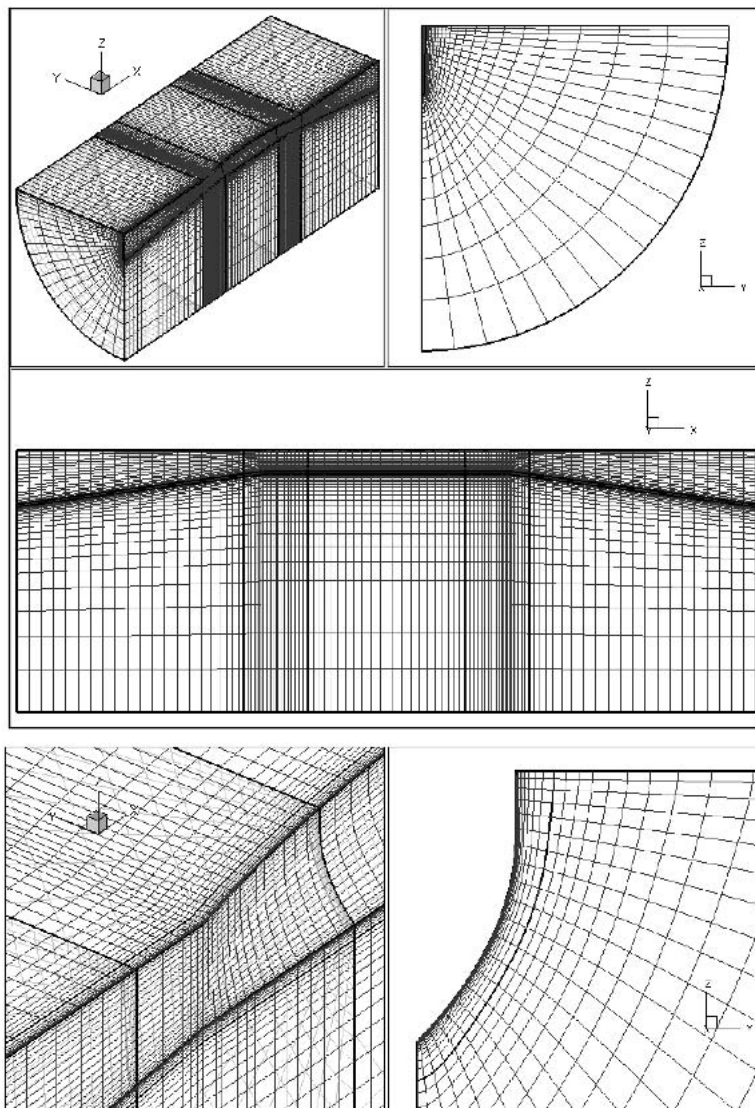


**Fig. 6** Coarse computational grid

moments. Motion coefficients are designated  $Y_i$  with the same index notation. In this work, the coefficients used are defined as

$$\begin{aligned} C_1(t) &= \frac{F_{b_1}(t)}{\zeta_a k \rho g \nabla}, C_3(t) = \frac{F_{b_3}(t)}{\zeta_a \rho g A_w}, C_5(t) = \frac{M_{b_1}(t)}{\zeta_a k \rho g I_{Ay}} \\ Y_3(t) &= \frac{x_{b_3}(t)}{\zeta_a}, Y_5(t) = \frac{\theta_{b_2}(t)}{\zeta_a k} \end{aligned} \quad (12)$$

where the ship geometry constants  $L$ ,  $\nabla$ ,  $A_w$ , and  $I_{Ay}$  are the ship length, the static displacement volume, the static waterplane area, and the waterplane pitch moment of inertia, respectively, and are found in Table 3.

Harmonic analysis of the time history values defines a periodic signal as

$$y(t) = \sum_n y^n \cos(n\omega_e t + \varepsilon_y^n) \quad (13)$$

where  $y^n$  is the  $n$ th harmonic amplitude, and  $\varepsilon^n$  is the  $n$ th harmonic

phase lag, which is taken to be relative to the wave elevation at the center of gravity of the model measured in degrees.

## Verification and validation

Convergence studies for grid spacing and time step were undertaken to assess numerical errors and uncertainties with grid and time step sizes given in Table 1. For the grid study, 100 time steps per wave period were used to obtain solutions on the fine, medium, and coarse grids. For the time step study, the finest grid was used to obtain solutions with 70, 100, and 140 time steps per wave period. Later, numerical errors and uncertainties are used during validation to assess modeling error and uncertainties when comparing solutions to benchmark data. The resonant physical conditions of the base case were chosen for these studies because the large ship motions and accelerations are likely to result in the highest numerical sensitivity, making this a worst-case test.

The verification parameters of the first harmonic longitudinal resistance and pitch and heave motions for the grid spacing con-

vergence study are given in Tables 4 and 5. Subscripts on force and moment coefficients refer to the degree of freedom (e.g.,  $i = 3$  refers to heave motion), while superscripts denote solutions on the finest grid. The resistance force exhibits a grid order of accuracy  $p_G$  of 1.95, which matches well with the expected order of the core unsteady flow solver. The other degrees of freedom, which are unrestrained, show more sporadic orders of accuracy, 3.09 and 2.59. It should be noted that higher order of accuracy does not imply higher accuracy, only that the simulated values converged more rapidly than expected. This may be due to the free surface treatment that conforms the grid to the unsteady free surface at every time step, making it impossible to guarantee true similarity from one grid to the next. Regardless, the values are not unreasonable for such a complicated simulation. Reasonably small levels for uncertainty  $U_G$  (2.84%, 0.73%, 1.32%) are predicted for the force, heave, and pitch coefficients, respectively.

Tables 6 and 7 show the verification parameters for the time step study. The tests were performed using the base case physical parameters and the fine grid. Time orders of accuracy  $P_T$  (1.19, 1.61, and 1.96) are close to the expected second order of the solver. The uncertainty levels are larger than those in the grid study, especially the longitudinal force coefficient, which suggests that the system is especially sensitive to time step size at this near-resonant case. However, if the steady resistance were used to normalize this longitudinal uncertainty, the value would be on the order of the other coefficients. Overall, numerical verification has been demonstrated for this most difficult case.

Corrected and uncorrected validation parameters of the first harmonic of coefficients are shown in Table 8. The uncertainty in Journee's experimental data is not given, and the fairly low value of  $U_D = 2.5\%$  has been assumed. Because the comparison error  $E$  is less than the validation uncertainty  $U_V$ , the longitudinal resistance and pitch motion have been validated for both the corrected and uncorrected case, at uncertainty levels of 4.45% and 2.52%, respectively. The heave motion has not been validated, with an error of 6.56% and an uncertainty of only 6.52%. However, correction of the heave motion has reduced the error to 5.89%.

Although the heave motion coefficient is just outside the range of validation, the uncertainty tests have garnished satisfactory results. It is with confidence then that we move on to the analysis of the predicted and prescribed motions results.

### Physical parameter studies

To investigate the response of the model over a range of Froude numbers, wavelengths, and wave heights, a limited number of physical parameter studies were undertaken. Figure 7 shows the predicted motion harmonic amplitudes and phase angles as a function of wavelength along with the first harmonic experimental data presented by Journee. The match is quite good, with the difference

**Table 4 Grid convergence study: results for first harmonic amplitudes of force and motion coefficients**

	Coarse (3)	Medium (2)	Fine (1)	$\varepsilon_{32} * 100$	$\varepsilon_{21} * 100$	Data
$C_1^1$	0.1167	0.1231	0.1264	-0.64	-0.33	0.118
$Y_3^1$	1.1737	1.1910	1.1969	-1.73	-0.59	1.28
$Y_5^1$	2.1137	2.1676	2.1897	-5.40	-2.20	2.21

**Table 5 Grid convergence verification of first harmonic amplitudes of force and motion coefficients**

	$p_G$	$C_G$	$U_G$	$\delta_G^*$	$U_{G_C}$
$C_1^1$	1.95	0.97	2.84%	-2.58%	0.09%
$Y_3^1$	3.09	1.92	0.73%	-0.49%	0.24%
$Y_5^1$	2.59	1.45	1.32%	-1.01%	0.31%

**Table 6 Time step convergence study: results for first harmonic amplitudes of force and motion coefficients**

	Coarse (3)	Medium (2)	Fine (1)	$\varepsilon_{32} * 100$	$\varepsilon_{21} * 100$	Data
$C_1^1$	0.1398	0.1264	0.1187	1.34	0.77	0.118
$Y_3^1$	1.1786	1.1969	1.2090	-1.83	-1.21	1.28
$Y_5^1$	2.1760	2.1897	2.1966	-1.36	-0.69	2.21

**Table 7 Time convergence verification of first harmonic amplitude of force and motion coefficients**

	$p_T$	$C_T$	$U_T$	$\delta_T^*$	$U_{T_C}$
$C_1^1$	1.61	0.75	21.44%	10.60%	3.62%
$Y_3^1$	1.19	0.51	5.97%	-1.53%	1.48%
$Y_5^1$	1.96	0.97	0.68%	-0.62%	0.02%

**Table 8 Validation of longitudinal force, heave, and pitch motion for fine grid**

	$U_{SN}$	$U_D$	$U_V$	$E$
$C_1^1$	21.63%	2.50%	21.77%	-0.84%
$C_{1C}^1$	3.68%	2.50%	4.45%	0.15%
$Y_3^1$	6.02%	2.50%	6.52%	6.56%
$Y_{3C}^1$	1.52%	2.50%	2.92%	5.89%
$Y_5^1$	1.48%	2.50%	2.91%	2.28%
$Y_{5C}^1$	0.31%	2.50%	2.52%	-1.28%

less than the estimated experimental uncertainty of 2.5% in all but the heave motion resonant case. From the verification study above, a finer time step would have increased the accuracy of the heave motion result greatly. However, the coarse time step has still provided excellent results overall. The zeroth order components of heave and pitch are the simulated sinkage and trim of the vessel. Journee did not supply sinkage and trim data, but it is well known that these effects are not generally a function of wavelength, and the results match this expectation.

Figure 8 shows the simulated motions response as a function of Froude number, again with the experimental data from Journee included for comparison. The pitch and heave motions and phase angles match extremely well with the experimental data, again with most deviations less than the likely uncertainty of the data. In addition, the computed sinkage and trim of the Wigley hull correspond well with qualitative expectations, with increased sinkage and stern trim at increased Froude numbers.

The final test run was to verify the linear response of the ship model to wave height. Nearly identical response coefficients were recorded for the two heights measured, just as they were by



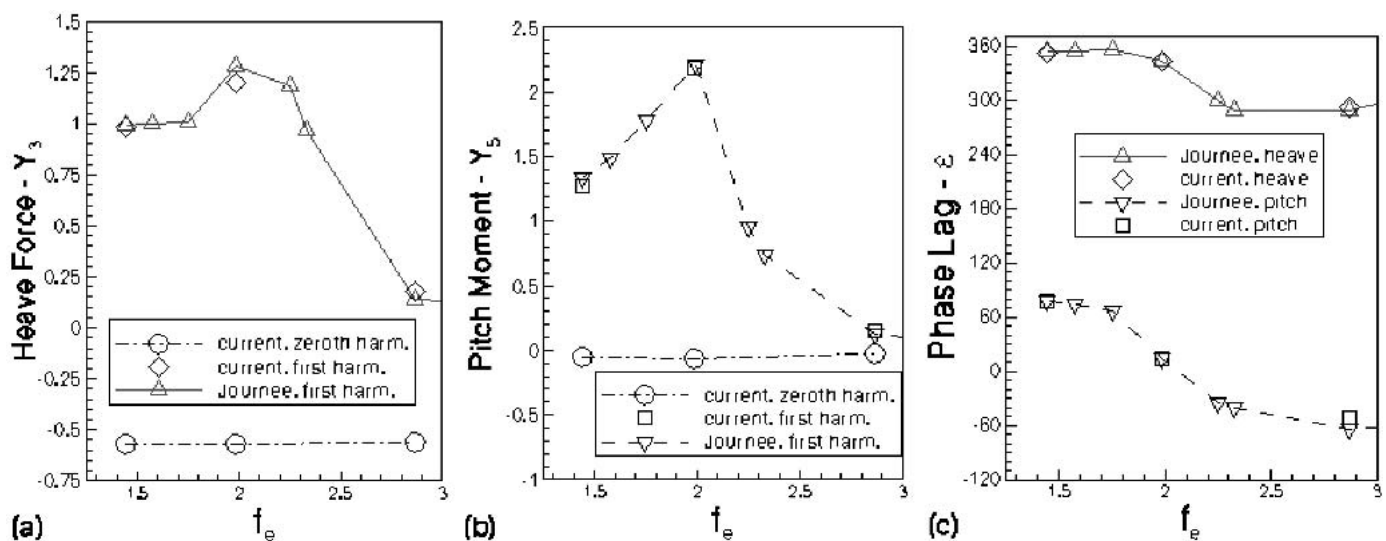


Fig. 7 Wavelength study: harmonic amplitudes of (a) heave motion, (b) pitch motion, and (c) harmonic phase angles of pitch and heave motion,  $Fr = 0.3$ ,  $\zeta_a/L = 3.67 \times 10^{-3}$

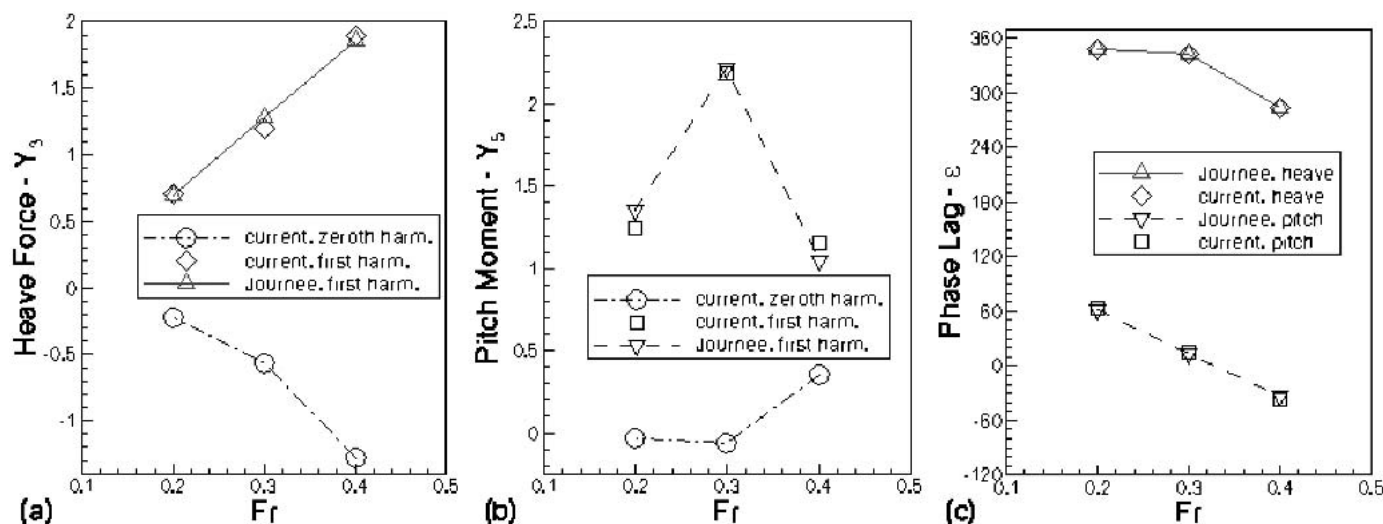


Fig. 8  $Fr$  study: harmonic amplitudes of (a) heave, (b) pitch, and (c) harmonic phase angles of pitch and heave motion,  $\lambda/L = 1.25$ ,  $\zeta_a/L = 3.67 \times 10^{-3}$

Journee. The values for this test along with the other simulation results generated in the physical parameter studies are shown in Table 9 along with Journee's experimental and strip theory simulation results.

Table 9 highlights the fact that the strip theory results are relatively accurate for the high- and low-frequency tests, as well as the lower Froude number. But for higher Froude number and the resonant frequency, the results are much less satisfactory. Also, strip theory is better at predicting heave than pitch overall.

### Unsteady free surface decomposition analysis

The complete flow fields were recorded for the last two periods of the predicted and prescribed motions tests. Figure 9 shows that section of the time history for the predicted base case motion with the wave height at the center of the model included for reference.

The time scale has been shifted such that the periods begin and end with the peak wave height at the center of gravity of the model.

Quarter period snapshots of the free surface elevation contours corresponding to the last encounter wave of the base case simulation are shown in Fig. 10. The incident wave clearly progresses from left to right in the figures: in Fig. 10a, the quarter period, the wave elevation at amidships is zero; in Fig. 10b it is minimum; in Fig. 10c it is zero; and at the full period in Fig. 10c the elevation at amidships is maximum.

The steady-state free surface elevation is compared to the mean of the unsteady free surface elevation for the base case in Fig. 11. The mean of the unsteady surface is similar to the steady surface, exhibiting a Kelvin wave pattern of similar proportion and magnitudes. The two surfaces are subtracted from each other in the bottom plot to highlight their differences. There is a shift in the wavelength in the unsteady case, giving rise to increased diver-

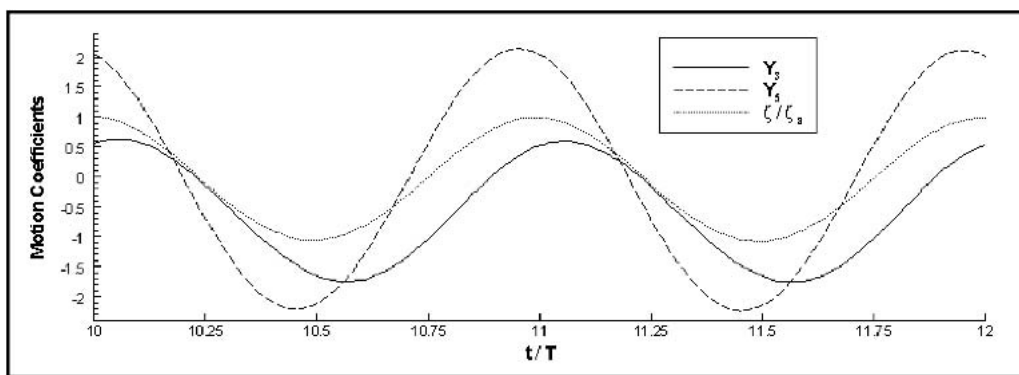


Fig. 9 Base case: predicted motions for last two periods

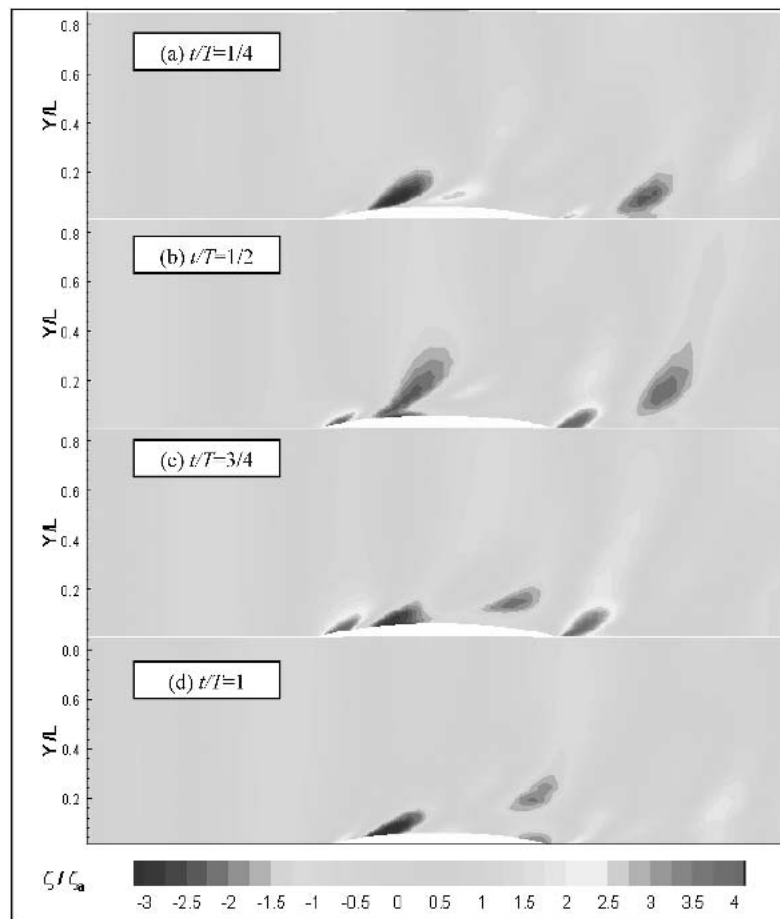


Fig. 10 Base case: unsteady free surface elevation at each quarter period. (a)  $t/T = 1/4$ . (b)  $t/T = 1/2$ . (c)  $t/T = 3/4$ . (d)  $t/T = 1$

gence moving in the positive  $x$  direction. However, the differences are an order of magnitude smaller than the surfaces elevations themselves within one ship length. The change in wavelength is due to the interaction between the traveling wave and the hull in predicted motions.

This interaction can be visualized more clearly by subtracting off the “steady” components of the free surface. Define the interaction surface  $\zeta_I$  by

$$\zeta_I(x, y, t) = \zeta(x, y, t) - \zeta_{\text{incident}}(x, t) - \zeta^0(x, y) \quad (14)$$

where  $\zeta_{\text{incident}}$  is the incident wave elevation given in equation (3) and  $\zeta^0$  is the mean elevation.

This unsteady surface shows only the effect of the hull-wave interaction and is presented in Fig. 12. A pattern of two alternating waves is observed. The high amplitude wave, 244% of the incident wave amplitude, forms on the bow shoulder, and the smaller wave, only 102% of the incident wave height, forms close to the trailing edge. These waves move slightly forward along the hull before detaching, moving in the direction of flow, and dissipating. This superposition of forward and reverse

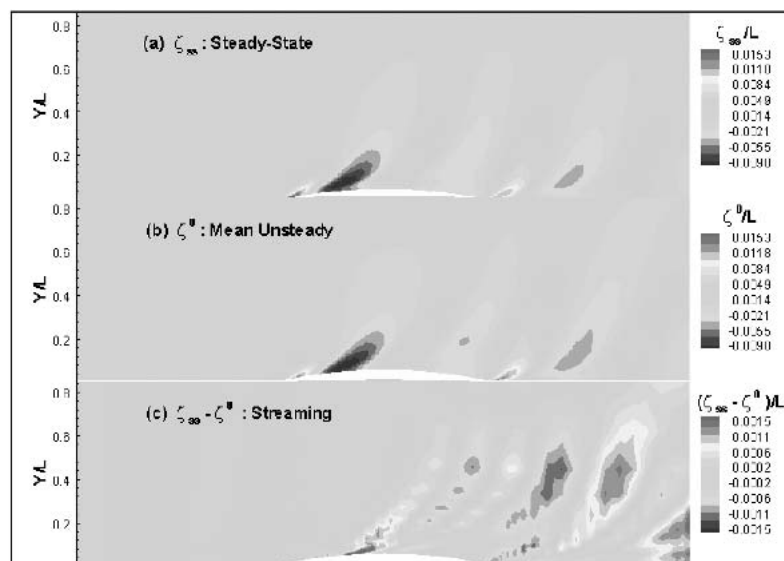


**Fig. 11** Base case: (a) steady-state, (b) mean unsteady, (c) streaming surface comparison

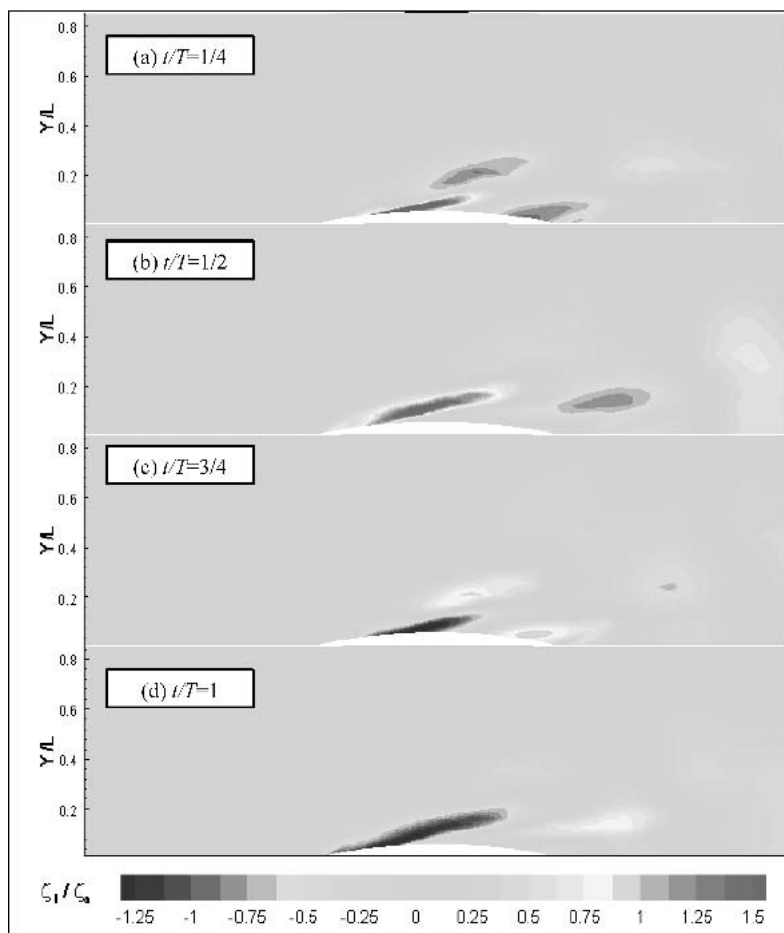


**Fig. 12** Base case: unsteady interaction wave elevation for each quarter period. (a)  $t/T = 1/4$ . (b)  $t/T = 1/2$ . (c)  $t/T = 3/4$ . (d)  $t/T = 1$

wave movement is exactly what would be expected of a pitch radiation wave in a uniform flow, but it makes interpretation of the harmonic phase angles of the unsteady free surface very difficult.

The harmonic amplitudes are quite clear, however, and are shown in Fig. 13. The first harmonic of the free surface is shown in the top plot, the first harmonic of the interaction wave is shown in the second plot, and the second free surface harmonic is shown

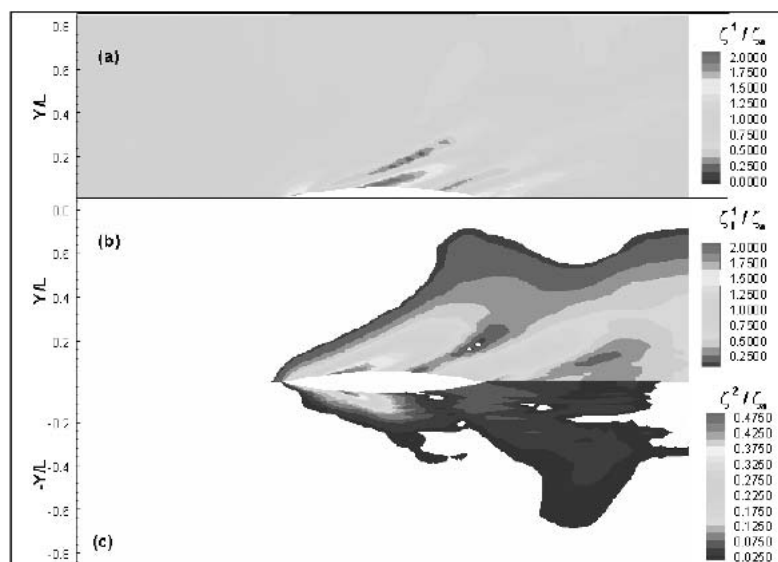


**Fig. 13** Base case: (a) free surface, (b) interaction surface first harmonic amplitude, (c) free surface second harmonic amplitude

in the bottom plot. From equation (14), it is clear that the mean of the interaction wave is zero and the second harmonic of the interaction wave will be the same as that of the original unsteady free surface.

The maximum amplitude of the unsteady free surface first harmonic is 197% of the incident wave height. The first harmonic of the interaction wave shows the same magnitude, but because the incident wave has been subtracted off, the pattern is quite different. The shoulder and trailing edge waves mentioned previously are clearly distinguishable. The second harmonic response has a lower magnitude, 49% of the incident wave height, but this is not negligibly small and there is a clear wave pattern similar to the first harmonic of the interaction wave.

### Unsteady boundary layer analysis

The unsteady boundary layer was recorded over the same period of time as the free surface. In Fig. 14, the underwater portion of the Wigley III hull is shown at four time slices during predicted pitch and heave motion simulations. In this view the bow is pointing to the right, and the wake is shown trailing off to the left. Slices of axial velocity have been taken along the length of the hull to show the unsteady boundary layer.

Unsteady viscous flow phenomenon, most notably the boundary layer bulge, which travels down the keel, are presented in this figure. Referencing Fig. 9 again, when the ship is at the extremes of its pitch and heave motion, a region of decelerated fluid develops at the keel, as shown in Fig. 14c. As the leading edge moves back down to its neutral position, the bulge is forced down the length of the keel. There are also large fluctuations in the leading and trailing edge effects over the wave encounter period. Although these qualitative observations are interesting, a detailed analysis of the boundary layer will require switching to a body-fixed reference frame and establishing a wall normal coordinate system.

The mean harmonic amplitude of the unsteady axial velocity is

compared to the steady-state solution in Fig. 15. The view in this plot is from directly under the hull, with the leading edge at the top and the trailing edge below. The points that did not remain wetted throughout the period have been deleted. The mean amplitude in Fig. 15b is similar to the steady solution shown in Fig. 15a, but the differences are highlighted when the two solutions are subtracted, as shown in Fig. 15c. There is a 5% decrease in flow speed near the keel, where the mean boundary layer has been expanded due to the traveling bulge mentioned earlier. Near the free surface, the boundary layer decreased relative to the steady flow, giving an increase in velocity of 13%.

The first and second harmonic amplitudes are shown in Fig. 16, similar to the free surface harmonic analysis. The first and second harmonics show similar patterns, but the second harmonic is more than an order of magnitude smaller. The maximum amplitudes are near the bow below the keel, where the traveling bulge originated, and at the trailing edge of the keel. All maximums occur relatively close to the hull.

To analyze viscous characteristics of this unsteady flow, the unsteady axial velocity profile at the centroid of the hull is shown in Fig. 17a using wall normal coordinates. The same four time slices used in the other snapshot plots are presented here, and although they show that the entire simulated boundary layer is unsteady, they fail to impart the serpentine nature of the profile motion.

The harmonic amplitudes of this profile are plotted in Fig. 17b. The mean of the unsteady axial velocity is a familiar-looking turbulent boundary layer plot. The first harmonic also seems intuitively correct, bringing to mind analytical solutions of the unsteady Navier-Stokes equations, such as harmonic pipe flow. Both the first and second harmonic amplitudes start at zero, as required by the no-slip condition, have local maxima at  $y^+ = 11$  and  $y^+ = 300$ , and then decrease until the edge of the boundary layer region is reached. At this point in the boundary layer the first harmonic is an order of magnitude smaller than the uniform velocity, and the second harmonic is two orders smaller. Figure 17c shows the

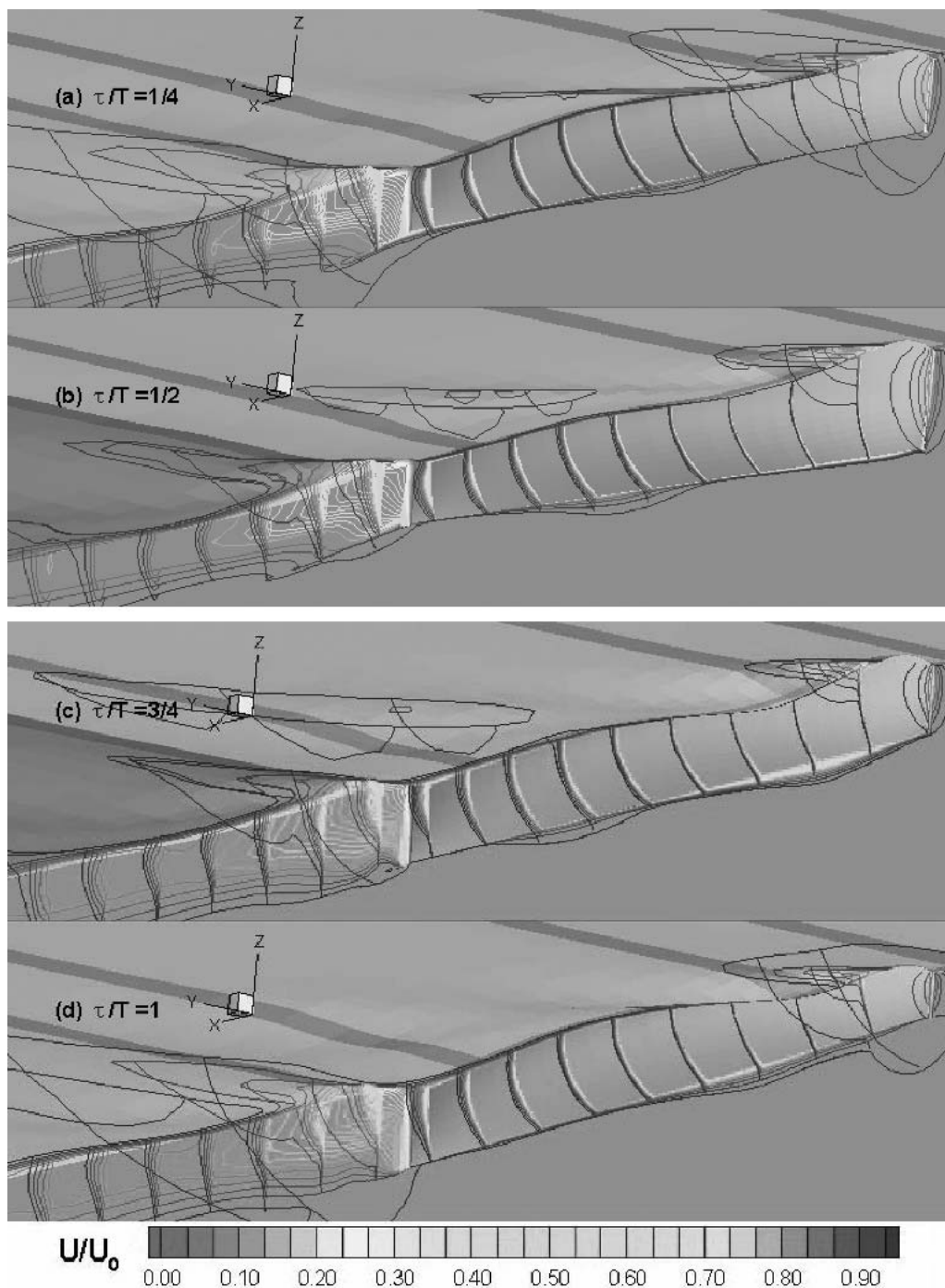


**Fig. 14** Predicted base case motions: slices of axial velocity contours for each quarter period

harmonic phase angles relative to the axial pressure gradient phase at the wall. The first harmonic fluctuation leads the pressure gradient by 110 deg near the wall, but the reaction phase is lowered steadily, moving out to the full boundary layer width until it lags by 70 deg around the boundary layer thickness. This steady phase shift is responsible for the serpentine motions mentioned above. The second harmonic phase is directly in phase with the axial pressure gradient near the wall, leading up to 60 deg at

$y^+ = 100$  and then lagging by 25 deg at the boundary layer thickness.

### Prescribed motion results

In this section the results for the forward speed diffraction (FSD), prescribed heave radiation (PHR), and prescribed pitch radiation (PPR) problems are presented and discussed.

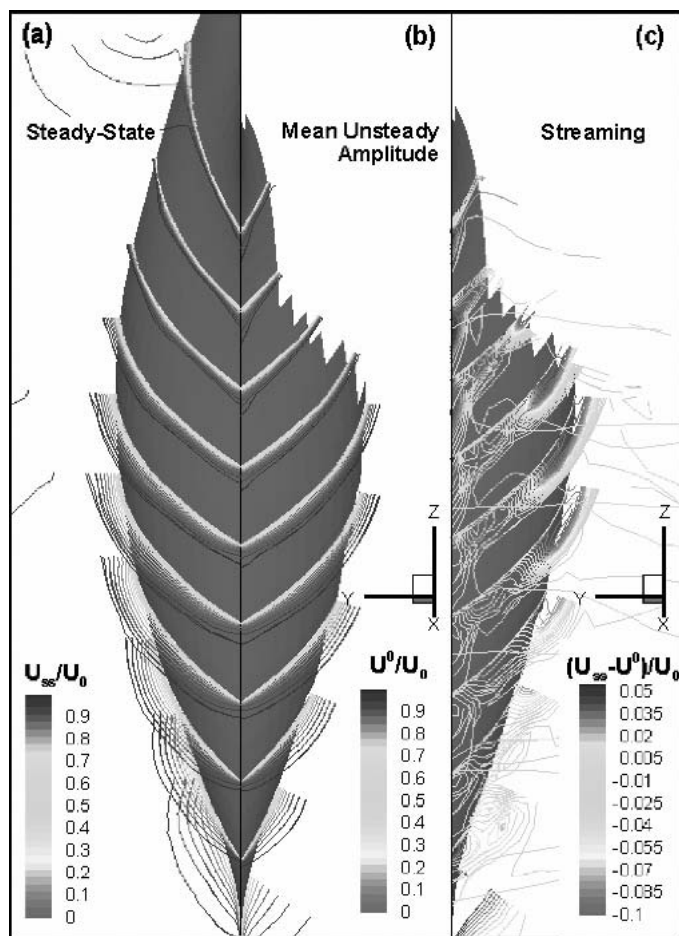


**Fig. 15** Base case: (a) steady-state, (b) mean unsteady, and (c) streaming axial velocity contour

### Strip theory equations

Strip theory takes the governing dynamic equations of motion given in equation (5) and linearizes the equations to the form

$$\begin{aligned} (m + a_{33})\ddot{x}_{b3} + b_{33}\dot{x}_{b3} + c_{33}x_{b3} + a_{35}\ddot{\theta}_{b2} + b_{35}\dot{\theta}_{b2} + c_{35}\theta_{b2} &= F_{w3} \\ (I_{yy} + a_{55})\ddot{\theta}_{b2} + b_{55}\dot{\theta}_{b2} + c_{55}\theta_{b2} + a_{53}\ddot{x}_{b3} + b_{53}\dot{x}_{b3} + c_{53}x_{b3} &= F_{w5} \end{aligned} \quad (15)$$

In this equation,  $F_w$  is the wave excitation force and moment, not the total force  $F_b$ . The  $b_{ij}$  coefficients are responsible for hydrodynamic damping and the  $a_{ij}$  coefficients are added mass terms. From equation (15) it is clear that the  $c_{ij}$  coefficients are the coefficients of hydrostatic restoring force and are functions of the model geometry only, not the flow conditions. For the Wigley III hull used in Journee's experiments, the coefficients are given by

$$\begin{aligned} c_{33} &= \rho g A_w = 6,119(N/m) \\ c_{55} &= \rho g I_{Ay} = 2,874(Nm) \\ c_{35} &= c_{53} = 0 \end{aligned} \quad (16)$$

The bulk of the strip theory method goes toward determining the hydrodynamic coefficients to use in these equations. For comparison purposes, the first harmonic amplitude and phase angle from a time-domain computational model or experimental data can be

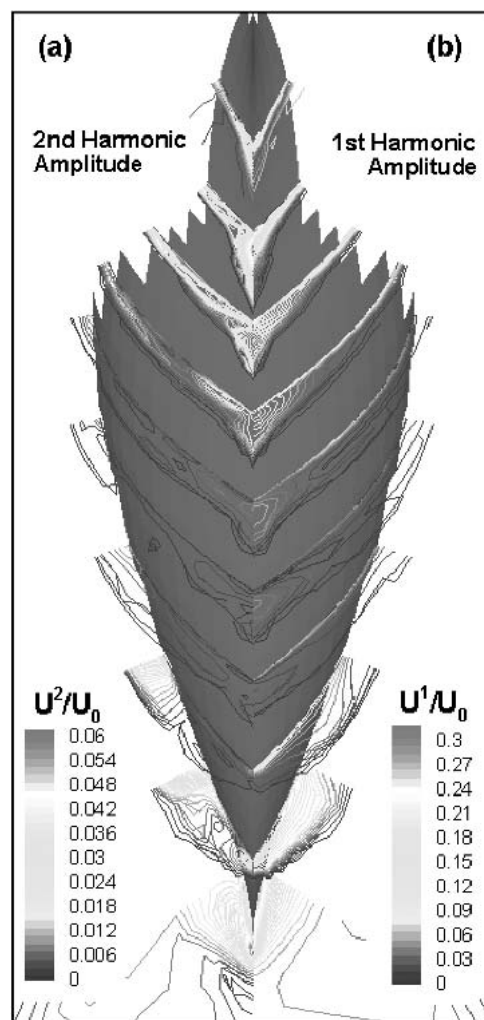


**Fig. 16** Base case: (a) second and (b) first unsteady axial velocity harmonic amplitudes

used to calculate the equivalent hydrodynamic coefficients and wave excitation force.

### Forward speed diffraction

The equivalent wave excitation force is calculated from the forward speed diffraction model problem. The Fourier transform (FT) of the harmonic amplitudes is simulated from the FSD test shown in Fig. 18, where the forces are plotted versus the harmonic,  $n$ , not the frequency. The pitch moment and heave force results are nearly completely linear, which agrees with measurements of the forward speed diffraction forces and moments presented in Gui et al (2002) for the 5415 naval surface combatant at this wavelength and Froude number. For these test conditions, the results show that it would be possible for a linear theory to model the forces.

Excitation force results are compared for various methods in Table 10. The strip theory results are taken from Journee (1992), and the SWAN results are taken from Rhee and Stern (2001). The sign of the cross coefficients is changed to match the coordinate

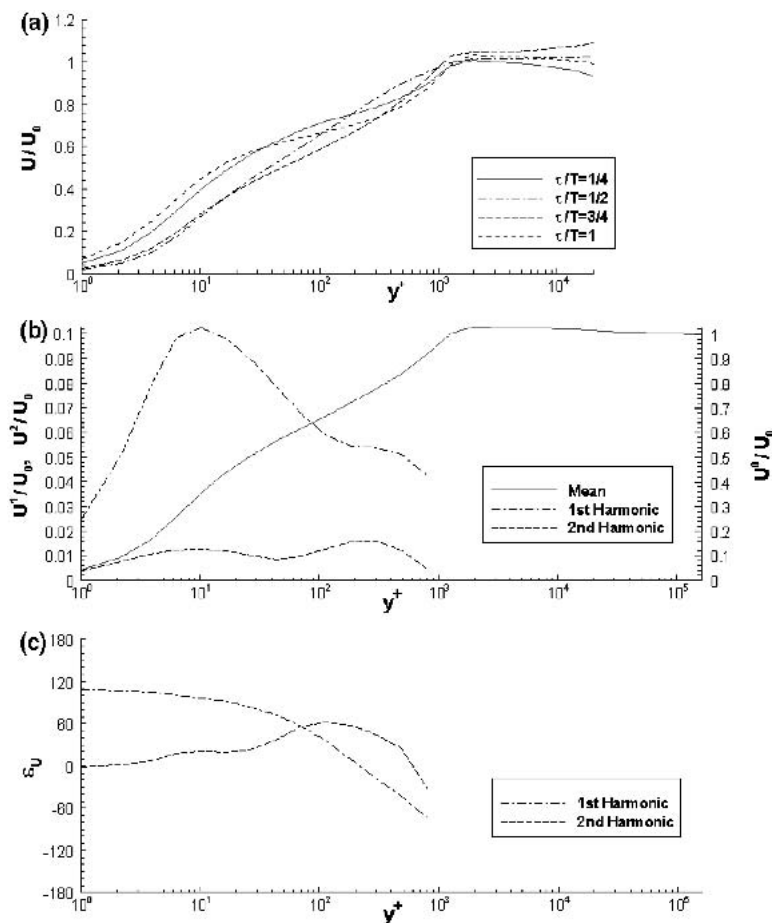


Fig. 17 Base case unsteady boundary layer profiles: (a) snap shots, (b) harmonic amplitudes, and (c) harmonic phase angles

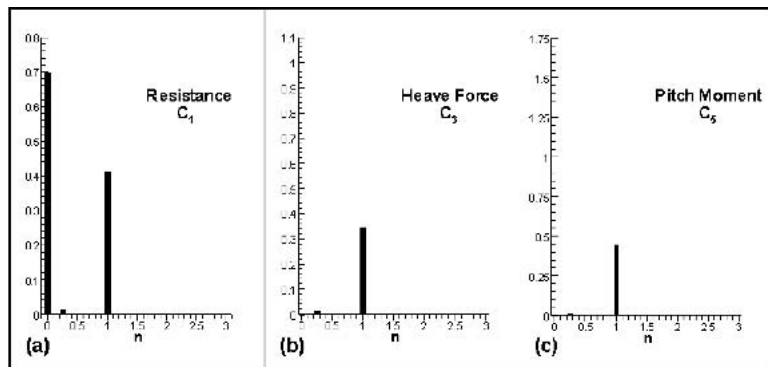


Fig. 18 Forward speed diffraction: (a) longitudinal force, (b) heave force, and (c) pitch moment

system used in Journee. The results for all four computational methods are fairly good, but the current work best simulates all of the compared experimental values other than the longitudinal force phase angle and the pitch force amplitude. The inviscid programs have the most trouble predicting the heave force with errors of 26% and 22% for SWAN and strip theory, respectively. However, it should be noted that for the full range of strip theory results provided in Journee, the results for  $\lambda = L$  were the least accurate. This is because strip theory is a matching method, join-

ing the short wavelength and long wavelength asymptotic solutions.

### Forward speed radiation

Next, the forward speed radiation tests are considered. Figures 19 and 20 show the resulting harmonic amplitudes for the PHR and PPR simulations. Because there is no incident wave in these tests, the results have been normalized using the base case values for  $\lambda$  and  $\zeta_a$ . Figure 19 shows that in addition to the expected

**Table 9** Experimental and simulation results for physical parameter studies

	$C_1^I$	$\varepsilon_{C1}^I$	$Y_3^I$	$\varepsilon_{Y3}^I$	$Y_5^I$	$\varepsilon_{Y5}^I$
Base case <i>MMLHL</i> *						
Exp.	0.118	165	1.28	343	2.21	13
Current	0.1264	16	1.1969	343	2.1897	14
S.T.	0.42	85	1.31	343	1.5	45
Low $\lambda$ <i>MLLHL</i> *						
Exp.	0.680	81	0.99	353	1.34	77
Current	0.6775	69	0.9817	352	1.2660	77
S.T.	0.68	81	1.0	360	1.2	77
High $\lambda$ <i>MHLHL</i> *						
Exp.	0.123	178	0.14	288	0.12	-65
Current	0.1010	188	0.1800	291	0.1533	-51
S.T.	0.05	180	0.02	250	0.12	-70
High $\zeta_a$ <i>MLHHL</i> *						
Exp.	0.127	176	0.15	286	0.13	-63
Current	0.1100	188	0.1810	291	0.1492	-51
S.T.	0.05	180	0.02	250	0.12	-70
Low Fr <i>LMLHL</i> *						
Exp.	0.373	65	0.69	349	1.35	62
Current	0.3949	59	0.7024	348	1.247	64
S.T.	0.38	45	0.70	350	1.15	62
High Fr <i>HMLHL</i> *						
Exp.	0.429	126	1.86	283	1.05	-34
Current	0.4238	130	0.1896	284	1.1580	-37
S.T.	0.41	90	-2.1	280	-1.75	-35

\*Values ( $L$ ,  $M$ , or  $H$ ) for five parameters Fr,  $\lambda$ ,  $\zeta_a$ , grid point, and time step as defined in Table 1.

heave force first harmonic, the forced heave oscillations have resulted in a small contribution to the resistance first harmonic, and very small second-order heave and first-order pitch responses.

There are more nonlinear responses to the forced pitch oscillations, as shown in Fig. 20. The first harmonic resistance response is very large, and there are smaller but significant first and second heave force responses. These nonlinear responses would be impossible for a linear theory to predict directly and result in our simulation results only because the fully nonlinear time-dependent equations were solved, even for the prescribed motions problems. By simplifying equations (15) for heave or pitch motion only, the equivalent hydrodynamic coefficients can be isolated. The coefficients resulting from the heave tests are given by

**Table 10** FSD forces and moments comparison

	Journee Exp.	Current	Rhee	SWAN	Strip Theory
$C_1^I$	0.259	0.261	0.253	0.215	0.209
$\varepsilon_{C1}^I$	109	102	103	107	100
$C_3^I$	0.205	0.201	0.211	0.151	0.160
$\varepsilon_{C3}^I$	41	30	16	29	25
$C_5^I$	0.316	0.308	0.335	0.275	0.312
$\varepsilon_{C5}^I$	99	98	98	102	95

$$\begin{aligned}
 A_{33} &= -\frac{F_3 \cos(\varepsilon_{F3})}{z_a \omega_f^2 \rho \nabla} + \frac{A_w g}{\omega_f^2 \nabla} + \frac{m}{\rho \nabla} \\
 B_{33} &= \frac{F_3 \sin(\varepsilon_{F3})}{z_a \omega_f \rho \nabla \sqrt{g/L}} \\
 A_{53} &= -\frac{M_2 \cos(\varepsilon_{M2})}{z_a \omega_f^2 \rho \nabla L} \\
 B_{53} &= \frac{M_2 \sin(\varepsilon_{M2})}{z_a \omega_f \rho \nabla L \sqrt{g/L}}
 \end{aligned} \quad (17)$$

and the coefficients based on the pitch test are given by

$$\begin{aligned}
 A_{35} &= -\frac{F_3 \cos(\varepsilon_{F3})}{\theta_a \omega_f^2 \rho \nabla L} \\
 B_{35} &= \frac{F_3 \sin(\varepsilon_{F3})}{\theta_a \omega_f \rho \nabla L \sqrt{g/L}} \\
 A_{55} &= -\frac{M_2 \cos(\varepsilon_{M2})}{\theta_a \omega_f^2 \rho \nabla L^2} + \frac{I_{Ag}}{\omega_f^2 \nabla L^2} + \frac{I_{yy}}{\rho \nabla L^2} \\
 B_{55} &= \frac{M_2 \sin(\varepsilon_{M2})}{\theta_a \omega_f \rho \nabla L^2 \sqrt{g/L}}
 \end{aligned} \quad (18)$$

In these equations, the coefficients have been normalized as in Journee, and uppercase letters have been used to denote the non-dimensional hydrodynamic coefficients. The coefficients calculated in the current work are compared to Journee's experimental and linear inviscid calculations, and to Beck's nonlinear time-domain inviscid calculations in Table 11. Beck changed the sign of the cross coefficients in his results to match the coordinate orientation in Journee. This convention was also adopted in Table

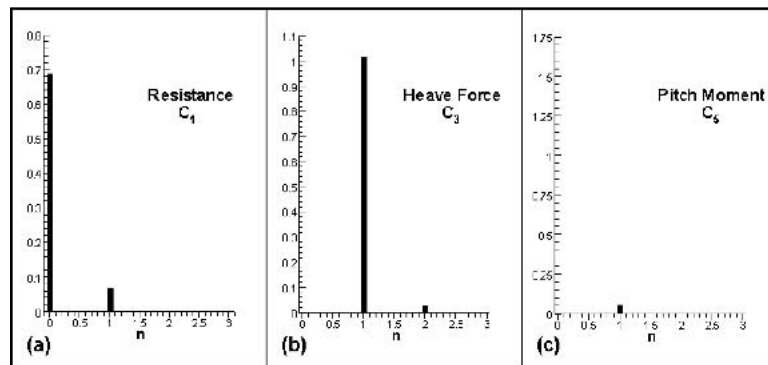


**Fig. 19** Forced heave oscillation test: (a) longitudinal force, (b) heave force, and (c) pitch moment



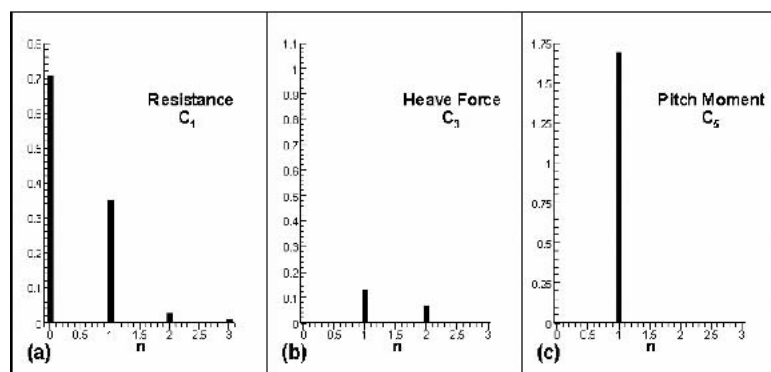


Fig. 20 Force pitch oscillations: (a) longitudinal force, (b) heave force, and (c) pitch moment

9. The strip theory coefficients are due to the method detailed in Salvesen et al (1970). The three-dimensional hybrid results were computed based on the zero forward speed code WAMIT and corrected for forward speed using Salvesen. The results for the linear inviscid codes, both strip theory and hybrid, are quite poor, with errors up to 200%. The nonlinear approach used by Beck shows dramatic improvement, although somewhat sporadically. The RANS approach used in this work has improved the results further and consistently.

## Summary and conclusions

In this work, an unsteady RANS method has been extended to model vertical plane ship dynamics through solution of the solid body equations of motion. The unsteady RANS method employed a surface tracking approach, and although this method was sufficient for the relatively small amplitude motions tested in the current work, very large amplitude motions will require a more robust method to avoid excessive grid distortion and grid generation constraints. Implementation of a fixed grid method, such as level set, is recommended for future work.

The predicted motions model was verified to be numerically convergent for force, moment, and motion coefficients through time step and grid spacing numerical refinement studies at the resonant case. The average error in force and motion coefficients during physical parameter studies was less than 2% when normalized by the maximum response. The free surface and boundary layer were decomposed using Fourier analysis and found to have structured higher-order responses.

In the forward speed diffraction tests, all the numerical models consulted reproduced the extremely linear exciting forces that

have been measured experimentally for simple hull forms at smaller Froude numbers and wave numbers. This was not the case for the radiation test results, however, for which the hydrodynamic coefficients generated by strip theory had comparison errors of up to 200%. Although a nonlinear inviscid method was shown to predict the hydrodynamic coefficients more accurately than the linear strip theory model, the current viscous method is still more accurate.

Inspection of the relative magnitude of these coefficients, however, leads to the conclusion that accurate prediction of the hydrodynamic coefficients is not required for accurate prediction of the pitch and heave motions of the hull. Hydrostatic coefficients  $c_{33}$  and  $c_{55}$  are at least an order of magnitude larger (and usually more than two orders larger) than the added mass and damping coefficients. The overwhelming dominance of hydrostatic restoring forces and highly linear wave excitation force allows the strip theory method to predict Wigley hull vertical plane motions with a reasonably high degree of accuracy.

However, there are limitations on these favorable conditions. For larger amplitude motions and more realistic hull geometries, a constant coefficient would be ill suited to predict the hydrostatic restoring forces even for simple pitch and heave motion. In such cases, nonlinear effects would need to be included. In addition, experimental studies have shown that for larger Froude numbers, larger wave numbers, and more complicated hull geometries, the wave excitation forces have large second harmonics. And, of course, for many physical systems, such as a ship in roll motion, the added mass and damping coefficients will have a relatively large magnitude. The current work suggests that unsteady RANS methods are well suited to accurately model these effects, although increased robustness in the numerical methods, as well as more detailed experimental measurements, will be required. It is recommended then that similar methods be used to model coupled vertical and horizontal plane motions, more complete wave spectrums, and more complicated hull geometries, toward the goal of a viable solution to the complete seakeeping problem.

## Acknowledgments

This research was sponsored by Office of Naval Research grant N00014-01-1-0073 under the administration of Dr. Patrick Purtell. The authors would like to acknowledge the Department of Defense High Performance Computing Modernization

Table 11 Comparison of nondimensional hydrodynamic coefficients

	Journee Exp.	Current	Beck	Strip Theory	3D Hybrid
$B_{33}$	1.994	1.950	1.750	2.150	2.225
$A_{53}$	0.034	0.035	0.034	0.085	0.085
$B_{53}$	-0.064	0.062	0.078	0.175	0.155
$A_{35}$	-0.041	0.046	0.036	0.086	0.086
$B_{35}$	0.059	0.060	0.061	0.150	0.178
$B_{55}$	0.064	0.063	0.057	0.116	0.089

Office and the Department of Defense Challenge Program. Simulations were performed at the Army Research Lab Major Shared Resource Center using both the SGI Origin 2000 and 3000 machines.

## References

- BECK, R., CAO, Y., SCORPIO, S. M., AND SHULTZ, W. 1994 Nonlinear ship motion computations using the desingularized method, *Proceedings*, 20th Symposium on Naval Hydrodynamics, August, Santa Barbara, CA, 227–246.
- CHEN, H. C., LIU, T., AND HUANG, E. T. 2001 Time-domain simulation of large amplitude ship roll motions by a chimera RANS method, *Proceedings*, 11th International Offshore and Polar Engineering Conference, June 17–22, Stavanger, Norway, vol. 3, 299–306.
- CURA HOCHBAUM, A., AND VOGT, M. 2002 Towards the simulation of sea-keeping and manoeuvring based on the computation of free surface viscous ship flow, *Proceedings*, 24th Symposium on Naval Hydrodynamics, July, Fukuoka, Japan.
- GUI, L., LONGO, L., METCALF, B., SHAO, J., AND STERN, F. 2002 Forces, moment, and wave pattern for naval combatant in regular head waves: part II: measurement results and discussions, *Experiments in Fluids*, **32**, 27–36.
- JOURNEE, J. M. J. 1992 *Experiments and Calculations on Four Wigley Hullforms*, Delft University of Technology, Ship Hydrodynamic Laboratory, Report No. 909, February.
- LARSSON, L., STERN, F., BERTRAM, V., EDITORS. 2000 *Proceedings*, Gothenburg 2000: A Workshop on Numerical Ship Hydrodynamics, Chalmers University of Technology, September, Gothenburg, Sweden.
- MILLER, R., GORSKI, J., AND FRY, D. 2002 Viscous roll prediction of a cylinder with bilge keels, *Proceedings*, 24th Symposium on Naval Hydrodynamics, July, Fukuoka, Japan.
- NEWMAN, J. N. 1988 *WAMIT Version 2.1, A Radiation-Diffraction Panel Program for Wave-Body Interactions*, Department of Ocean Engineering, Massachusetts Institute of Technology, Cambridge, MA.
- PATERSON, E. G., WILSON, R. V., AND STERN, F. 2003 *General Purpose Parallel Unsteady RANS Ship Hydrodynamics Code: CFDSHIP-IOWA*, IIHR Report 432, Iowa Institute of Hydraulic Research, University of Iowa, Iowa City, IA, November.
- RHEE, S., AND STERN, F. 2001 Unsteady RANS method for surface ship boundary layer and wake and wave field, *International Journal of Num. Meth. Fluids*, **37**, 445–478.
- SALVESEN, N., TUCK, E. O., AND FALTINSEN, O. 1970 Ship motions and sea loads, *Transactions of the Society of Naval Architects and Marine Engineers*, **78**, 250–287.
- SATO, Y., MIYATA, H., AND SATO, T. 1999 CFD simulation of 3-dimensional motion of a ship in waves: application to an advancing ship in regular head waves, *Marine Science and Technology*, **4**, 108–116.
- STERN, F., WILSON, R. V., COLEMAN, H., AND PATERSON, E. 2001 Comprehensive approach to verification and validation of CFD simulations—part 1: methodology and procedures, *ASME Journal of Fluids Engineering*, **123**, 793–802.
- TAHARA, Y., PATERSON, E., STERN, F., AND HIMENO, Y. 2000 CFD-based optimization of naval surface combatant, *Proceedings*, 23rd ONR Symposium on Naval Hydrodynamics, September, Val de Reuil, France.
- WEYMOUTH, G. 2002 *RANS CFD Predictions of Pitch and Heave Ship Motions in Head Seas*, MS thesis, Iowa Institute of Hydraulic Research, University of Iowa, Iowa City, IA.
- WILSON, R., PATERSON, E., AND STERN, F. 2000 Verification and validation for RANS simulation of a naval combatant, *Proceedings*, Gothenburg 2000: A Workshop on Numerical Ship Hydrodynamics, Chalmers University of Technology, September, Gothenburg, Sweden.
- WILSON, R., AND STERN, F. 1998 Unsteady RANS simulation of a surface combatant in regular head waves, *Proceedings*, 22nd Symposium on Naval Hydrodynamics, August, Washington, DC.
- WILSON, R., AND STERN, F. 2002a Verification and validation for RANS simulation of a naval surface combatant, *Proceedings*, 40th Aerospace Sciences Meeting and Exhibit, Reno, NV, January, AIAA 2002-0904.
- WILSON, R., AND STERN, F. 2002b Unsteady RANS simulation of a surface combatant in roll motion, *Proceedings*, 24th Symposium on Naval Hydrodynamics, July, Fukuoka, Japan.